Acta Oceanol. Sin., 2020, Vol. 39, No. 3, P. 63–72
https://doi.org/10.1007/s13131-020-1562-8
http://www.hyxb.org.cn
E-mail: hyxbe@263.net

Eddy covariance measurements of turbulent fluxes in the surf zone

Yongfeng Qi[1], Xiaodong Shang[1]*, Guiying Chen[1], Linghui Yu[1]

[1] State Key Laboratory of Tropical Oceanography, South China Sea Institute of Oceanology, Chinese Academy of Sciences, Guangzhou 510301, China

Received 4 July 2019; accepted 16 August 2019

Abstract

Turbulent eddies play a critical role in oceanic flows. Direct measurements of turbulent eddy fluxes beneath the sea surface were taken to study the direction of flux-carrying eddies as a means of supplementing our understanding of vertical fluxes exchange processes and their relationship to tides. The observations were made at 32 Hz at a water depth of ~1.5 m near the coast of Sanya, China, using an eddy covariance system, which mainly consists of an acoustic doppler velocimeter (ADV) and a fast temperature sensor. The cospectra-fit method—an established semi-empirical model of boundary layer turbulence to the measured turbulent cospectra at frequencies below those of surface gravity waves—was used in the presence of surface gravity waves to quantify the turbulent eddy fluxes (including turbulent heat flux and Reynolds stress). As much as 87% of the total turbulent stress and 88% of the total turbulent heat flux were determined as being at band frequencies below those of surface gravity waves. Both the turbulent heat flux and Reynolds stress showed a daily successive variation; the former peaked during the low tide period and the later peaked during the ebb tide period. Estimation of roll-off wavenumbers, k_0, and roll-off wavelengths, λ_0 (where $\lambda_0=2\pi/k_0$), which were estimated as the horizontal length scales of the dominant flux-carrying turbulent eddies, indicated that the λ_0 of the turbulent heat flux was approximately double that of the Reynolds stress. Wavelet analysis showed that both the turbulent heat flux and the Reynolds stress have a close relationship to the semi-diurnal and diurnal tides, and therefore indicate the energy that is transported from tides to turbulence.

Key words: eddy covariance, turbulent fluxes, surface gravity waves, cospectrum, tides

Citation: Qi Yongfeng, Shang Xiaodong, Chen Guiying, Yu Linghui. 2020. Eddy covariance measurements of turbulent fluxes in the surf zone. Acta Oceanologica Sinica, 39(3): 63–72, doi: 10.1007/s13131-020-1562-8

1 Introduction

Turbulent eddies play a critical role in most environmental fluid flows. The turbulent transfer of momentum by these eddies modifies larger-scale velocity fluctuations by transferring boundary forces through the water column (Kirincich et al., 2010). Heat and momentum that are transported by turbulent eddies from the surface to depth, dramatically affect the dynamics of the upper ocean. Furthermore, the heat and energy exchange that occurs between large-scale water masses in the oceans are completed through the interaction of eddies of differing scales. Thus, the direct observation of turbulent eddy fluxes is of great significance for improving the parameterization scheme of ocean models. High quality vertical eddy fluxes estimates are necessary to formulate and test hypotheses regarding the dynamics of ocean turbulence.

Turbulent eddy fluxes in fluid have been measured for decades (Priestley and Swinbank, 1947; Shang et al., 2003, 2004). One of the most commonly used methods is the eddy covariance technique, which measures the covariance between the turbulent fluctuations of the transported quantity of interest (e.g., horizontal momentum or temperature) and the fluctuations of vertical velocity (Bowden and Fairbairn, 1956; Heathershaw, 1979). Scientists have been using this technique to study the turbulent fluxes at the bottom boundary layer of the ocean and to study sediment transport in other natural aquatic environments, using for example Reynolds stress and turbulence values, oxygen uptake, submarine groundwater discharge, and dissolved organic carbon benthic flux (Berg et al., 2003, 2007, 2009; Kuwae et al., 2006; Crusius et al., 2008; Reimers et al., 2012; Yamamoto et al., 2015). Oceanographic research has focused largely on the bottom boundary layer; therefore, few studies have reported on the eddy heat flux transported within the ocean (Gerbi et al., 2008).

At the sea surface, surface gravity waves dominate the energy spectrum of the time series in most coastal ocean environments, with wave orbital velocities being orders of magnitude greater than those of turbulent eddies. Thus, small but unavoidable errors in instrument orientation can result in wave-induced fluxes, which are much larger than the eddy fluxes themselves (Trowbridge, 1998). Therefore, the use of the eddy covariance technique is limited in the presence of surface gravity waves. Direct measurements of turbulent fluxes in the ocean with the effects of surface gravity waves have become reliable only recently. Shaw and Trowbridge (2001) estimated near-bottom, turbulence-induced eddy fluxes in the presence of energetic wave motions with

Foundation item: The National Natural Science Foundation of China under contract Nos 41876023, 41630970 and 41876022; the Instrument Developing Project of the Chinese Academy of Sciences under contract No. YZ201432; the Guangzhou Science and Technology Project under contract No. 201707020037; the National Key R&D Plan of China under contract Nos 2017YFC0305804 and 2017YFC0305904.

*Corresponding author, E-mail: xdshang@scsio.ac.cn

a current meter array. Gerbi et al. (2008) developed the cospectra-fit method and successfully measured heat and momentum budgets across the air-sea interface in the mixed layer and assessed the ability of rigid-boundary turbulence models beneath the surface of the ocean. They found that the dominant horizontal length scales of flux-carrying turbulent eddies were consistent with observations from the bottom boundary layer of the atmosphere and from laboratory experiments. Recently, in applying the cospectra-fit method, Kirincich et al. (2010) used velocity observations from acoustic doppler current profilers (ADCPs) to estimate turbulent Reynolds stress in estuaries and tidal channels. Trowbridge et al. (2018) studied the cospectrum of stress-carrying turbulence in the presence of surface gravity waves, and revealed that the advection of standard boundary-layer turbulence (from random oscillatory velocities produced by surface gravity waves) causes cospectra in the ocean to differ from the shape that has been established for the atmospheric surface layer.

Although turbulent eddy fluxes have been widely studied in coastal regions, time series of turbulent eddy fluxes on a daily basis have not been reported to date. Questions relating to how the length scales of flux-carrying eddies contribute to eddy fluxes are also unclear. Furthermore, the relationship between the tides and turbulence eddy fluxes, including heat flux and Reynolds stress, is still unknown. Tides are the basic dynamic characteristics of the coastal ocean, and they have been verified as enhancing the dissipation of turbulence and material exchange at the coastal boundary layer (Lozovatsky et al., 2008). Routine estimates of turbulent eddy fluxes in tidal flows would help in the evaluation of turbulence closure methods used in ocean numerical models, as the former represent one of the largest sources of uncertainty in the latter (Warner et al., 2005).

In this study, we observed the surf zone for two days and measured vertical turbulent eddy fluxes using an eddy covariance system. The aim was to study the length scales of eddies responsible for the transportation of vertical fluxes, including heat and momentum, beneath the air-sea interface. We also addressed the relationship between small-scale turbulent eddy fluxes and large-scale tides.

2 Materials and methods

2.1 *Instrument and measurement*

Measurements were conducted in the surf zone on the coast of Sanya, China (18.22°N, 109.49°E, Fig. 1), over two days from midday 5 September to 7 September 2013. Measurements were made using an eddy covariance system consisting of an acoustic doppler velocimeter (ADV; Vector-300, Nortek AS, Norway) and a high-frequency sampling temperature probe. The eddy covariance system was secured beneath the sea surface at a depth of ~1.5 m using a steel pole that had been fixed firmly to the seabed. The total water depth of the observation station was ~4 m.

An ADV can measure three velocity components (u, v, and w) at a frequency as high as 64 Hz, although the sampling frequency can also be set to 1, 2, 4, 8, 16, or 32 Hz. Velocities were measured in a small cylindrical volume (~1.5 cm long and ~0.6 cm in diameter) located 15 cm away from three signal transmitters (Fig. 1). The velocity measurement range was 0.01–7.0 m/s, with an accuracy of ± 0.5%, which ensured an accurate measurement of ocean turbulence. An inertial measurement unit was installed in the ADV to measure the earth's magnetic field and the acceleration matrix of nine components. As it includes a tilt sensor, the instrument could obtain heading information and could convert velocity measurements to earth coordinates (E, N, and U). The ADV also recorded temperature (a low frequencies), pressure, and other variables for data quality selection.

An independently developed high-speed sampling temperature probe was used in the system for simultaneously measuring the ocean temperature, and was installed outside of the focused cylindrical volume of sonic pulse launched by the transmit transducers of the ADV. We note that it was not possible to position the temperature probe inside the focused cylindrical volume, as we wanted to avoid the false echoes of the physical object. However, the focused cylindrical volume and the temperature probe had to remain within a certain distance of each other in order to capture the same eddies of turbulence. The temperature probe had a response time of 7×10^{-3} s, the accuracy to reach 2×10^{-3}℃, and a sampling frequency of up to 143 Hz.

In this study, the system was setup to the continuously recording model, and energy was supplied by external batteries. The sampling frequencies of the ADV and temperature probe were set to 32 Hz.

2.2 *The surface gravity wave and tidal currents*

The observation system was secured in the surf zone, hence the collected data was inevitably affected by surface waves. We did not measure surface waves directly, however, this information can be extracted by processing the pressure signal recorded by the ADV. Firstly, the pressure signal was processed by one-

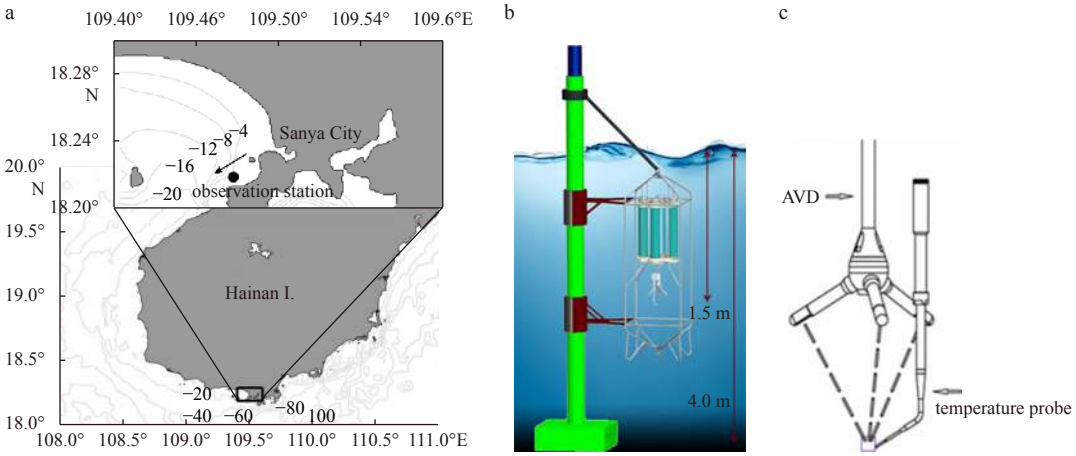

Fig. 1. Location of the measurement site (a), Diagram of observation system secured in the surf zone (b), and the mounting position of ADV and temperature probe(c). The arrow in the inset of (a) indicates the tidal current direction.

second low-pass filtering because of the low resolution of the pressure sensor (~0.02×10⁴ Pa) on the ADV (Fig. 2a). The low-pass filtered data was then handled by five-minute high-pass filtering (Fig. 2b), where the remainder indicates the effective wave heights. Figure 2b shows that, during the period of observation, the effective wave heights were within 0.3 m, and were smaller in the nighttime in comparison to those in the daytime. The wave periods mainly ranged from 3–7 s (Fig. 2a).

The semi-diurnal tide and diurnal tide signals were recorded by the pressure sensor on the ADV, thus the water level fluctuated twice a day (Fig. 2c). In our measurements, the tidal currents were relatively small, with the maximum component velocity <0.1 m/s (Fig. 2d). The direction of the tidal currents was towards the southwest, which is parallel to the shoreline (arrow on the left-hand side of Fig. 1). The ebb tide and low tide periods are marked in Fig. 2 for the purpose of analysis (Section 3.2).

In the assumption of linear surface waves, the pressure signal measured beneath the sea surface is highly related to the velocity measurements (Mei, 1989). Figure 3a plots the vertical velocity measured by the ADV in a 50 second segment and the partial derivative of pressure versus time. Before the derivative processing of the pressure data, the pressure signal was processed by low-pass filtering for one second for its low resolution (Fig. 2a). Vertical velocity was constant with the partial derivative of pressure, with a linear fit coefficient of determination (R^2) of 0.45, thus indicating that the gravity surface waves induced motion. If the influence of surface waves is not excluded, the resultant turbulent fluxes are unacceptable (Gerbi et al., 2008).

2.3 *Original eddy heat flux*

In the analysis, instantaneous values of temperature and velocity in the x, y, and z directions are denoted by T and u, v, and w, respectively. Because of the influence of surface waves, the velocity and temperature observations were decomposed into

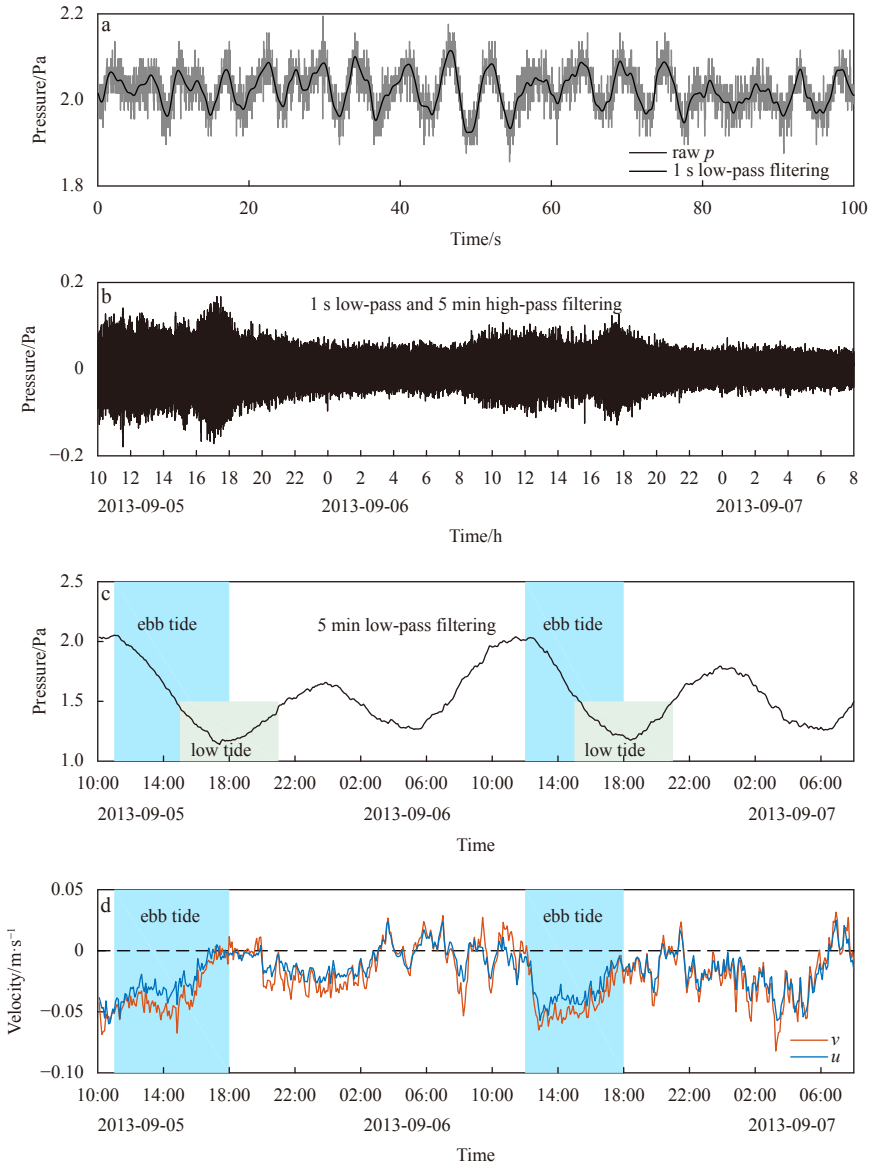

Fig. 2. The pressure and velocities were recorded by the ADV. One segment of raw pressure and 1 s low-pass filtering signals at 2013–09–05 10:00 (a), the pressure signal with 1 s low-pass and 5 min high-pass filtering processes (b), indicating the effective wave height, the pressure signal with 5 min low-pass filtering, indicating the depth of the instrument (c), and zonal velocities (d), respectively.

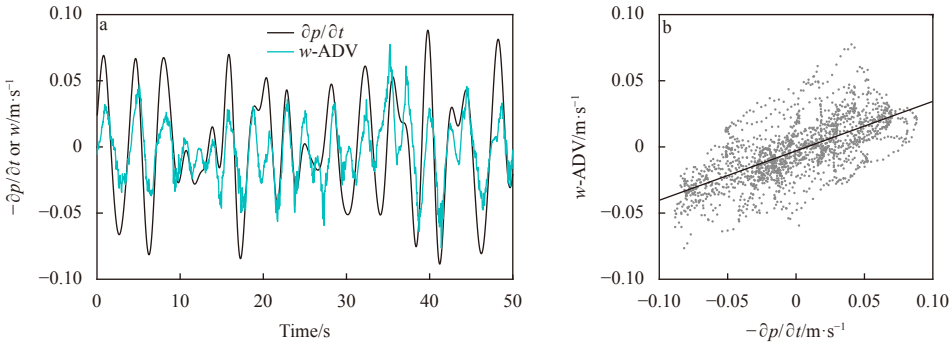

Fig. 3. An example of the effect of surface waves on the vertical velocity measurement. a. Comparison of the vertical velocity, w, measured by the ADV and the partial derivative of pressure versus time, $-\partial p/\partial t$, and b. linear fitting between $-\partial p/\partial t$ and w, where the coefficient of determination, R^2, is 0.45.

mean, wave, and turbulent components, where the wave-induced motions are defined as those that are coherent with displacements of the free surface (Gerbi et al., 2008). The decomposition for u is expressed by Eq. (1):

$$\begin{aligned} u &= \overline{u} + \tilde{u} + u', \\ T &= \overline{T} + \tilde{T} + T', \end{aligned} \tag{1}$$

with u being replaced by v and w for their decompositions. The overbars represent a time mean over the time interval of flux calculation, $\tilde{T}$ and $(\tilde{u}, \tilde{v}, \tilde{w})$ denote wave-induced motions, and T' and (u', v', w') indicate turbulent components. We note that the mean values of wave-induced perturbations and turbulent perturbations are zero. In practice, we decomposed the signals of temperature and velocity into mean parts and fluctuation parts. The fluctuation parts of the signal were further decomposed into turbulent motions and wave motions. All the decompositions were considered in the time domain.

The vertical turbulent heat flux, Q_s, and the Reynolds stress, τ (i.e., momentum flux), are calculated with turbulent velocity and temperature covariances as shown by Eqs (2) and (3),

$$\tau = -\rho_0 \overline{u'w'}, \tag{2}$$

$$Q_s = \rho_0 C_p \overline{T'w'}, \tag{3}$$

where ρ_0 is the reference density and C_p is the specific heat of water. Here the calculations (including separation and time averaging) are made in 5 min intervals. Velocities in the time intervals were rotated into downstream coordinates using the mean flow velocity direction to fulfill the condition where $\overline{v} = 0$, thus only one direction of the Reynolds stress was considered.

2.4 *The cospectra-fit method*

It is difficult to derive the turbulent components of temperature and velocity with the influence of surface waves. Thus, the direct use of Eqs (2) and (3) is limited. If the wave-induced components are not excluded, the resulting covariances are typically one-two orders of magnitude larger than the values expected from the surface fluxes.

Gerbi et al. (2008) used an alternative approach, the cospectra-fit method, to successfully estimate the acceptable turbulent heat flux and Reynolds stresses from ADVs, deployed in the mixed layer during conditions in which surface gravity waves existed and direct covariance failed. This method assumes that the spectra of vertical velocity can be separated into the wave band and the below-wave band turbulent motions by determining a wave band cutoff frequency. Below this cutoff, motions are presumed to be dominated by turbulence, whereas above this cutoff, motions are caused by a combination of turbulence and the much more energetic surface waves. The method works by only considering the cospectrum of $\overline{u'w'}$ and $\overline{T'w'}$ at frequencies below the cutoff frequency, where the motions are dominated by turbulence, and it fits a model to the observed cospectrum at these frequencies to estimate the total stress and turbulent heat flux present. The cospectra-fit method assumes that a semi-theoretical prediction of turbulence cospectra—as based on studies of boundary layer turbulence in the atmosphere and oceans (Kaimal et al., 1972; Wyngaard and Coté, 1972; Soulsby, 1980)—appropriately describes the spectral shape of the Reynolds stress and heat flux.

The one-side model cospectrum is defined by Eq. (4):

$$Co_{\beta w}(k)^{model} = \overline{\beta' w'}^{model} \left(\frac{7}{3\pi} \sin\frac{3\pi}{7}\right) \frac{1/k_0}{1 + (k/k_0)^{7/3}}, \tag{4}$$

where β is u or T, and the model-derived stress, heat flux, and cospectra are denoted by "*model*". Here $k = 2\pi/\lambda$ is the wavenumber, λ is the wavelength, and k_0 is a measure of the dominant length scale of the turbulent fluctuations or the location of the peak of the variance-preserving cospectrum. The model turbulent cospectrum in Eq. (4) can be defined by two variable parameters: the model fitted covariance $\overline{\beta' w'}$, and the roll-off wavenumber, k_0. Spectra of the semi-theoretical model are approximately constant at small wavenumber and roll-off as $k^{-7/3}$ at a high wavenumber (Fig. 4a). Further explanation includes that the model describes turbulence created at a large length scale, approximate to $\lambda_0 = 2\pi/k_0$, that cascades to smaller scales in an inertial range with a logarithmic spectra slope of –7/3. A variance-preserving cospectrum is derived by multiplying the cospectrum by the wavenumber, k, where k_0 defines the peak of the model cospectrum (Fig. 4b). Additionally, the cumulative integral of the cospectrum (Fig. 4c)—the Ogive curve—increases with increasing wavenumber to a maximum value equal to the total Reynolds stress or turbulent heat flux at the highest wavenumbers. The Ogive curve is expressed by Eq. (5):

$$\overline{\beta' w'} = \int_0^{k_{\max}} Co_{\beta w}(k)\, \mathrm{d}k. \tag{5}$$

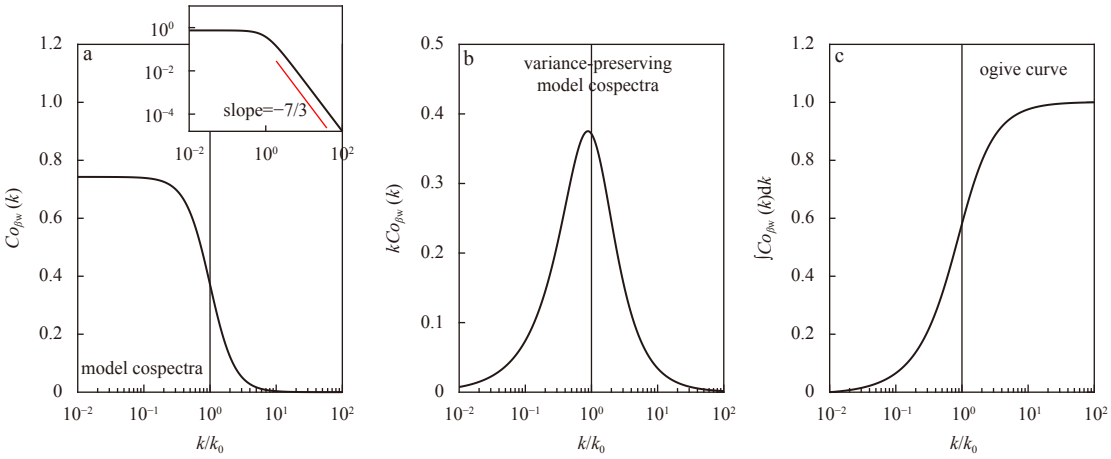

Fig. 4. Semi-theoretical model for boundary layer turbulence of cospectrum (a), variance-preserving cospectrum (b), and ogive curve (i.e., the cumulative integral of the model cospectrum) (c). The inset of (a) displays the log-log plot. $Co_{\beta w}(k)$ relates to $Co_{uw}(k)$ or $Co_{Tw}(k)$.

One of the most critical steps of Gerbi's cospectra-fit method is to identify the cutoff frequency ω_c ($\omega_c = k_c U$, where k_c is the cutoff wavenumber and U is the horizontal velocity), which separates velocities in the wave band from the below-wave band turbulent motions. k_c is a property of the wave field whereas k_0 is a property of the turbulence. The cutoff frequency is obtained by comparing the vertical velocity spectra, S_{ww}^{ADV}, which is derived from the ADV and the vertical velocity spectra, S_{ww}^{pres}, which in turn is derived from pressure measurements (Figs 5a1, b1). In our study, the pressure inferred vertical velocity was obtained by

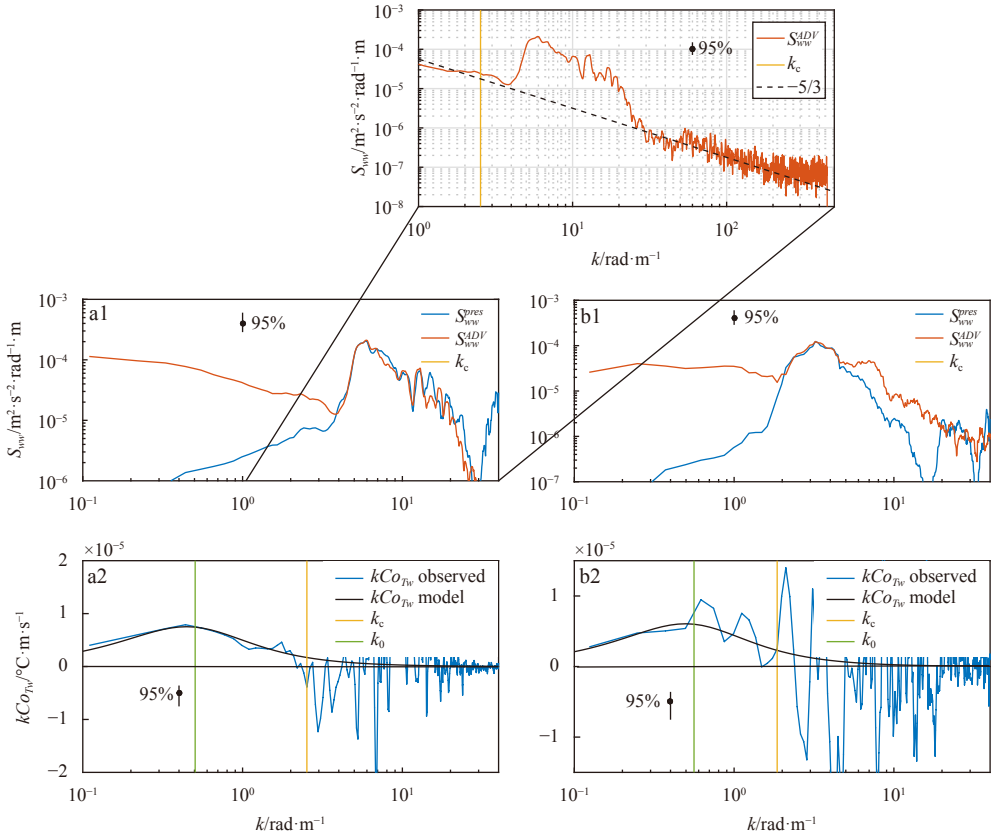

Fig. 5. Two examples of the cospectra-fit estimates. a1. Auto-spectra of vertical velocity fluctuations for a sample of a 5 min interval at 2013–09–06 22:40 local time. The blue line is the velocity spectrum recorded by ADV, and the red line is the spectrum derived from the difference of the pressure sensor. The vertical yellow line indicates the cutoff wavenumber k_c. The top inset shows the comparison of the auto-spectra and the –5/3 slope. The discrepancy is obvious in the surface wave band. a2. the corresponding variance-preserving cospectra of vertical velocity and temperature fluctuations. The blue line is the observed variance-preserving cospectra, and the dashed line is the model fitted with Eq. (4). The vertical green line is the peak of the model variance-preserving cospectrum. b1 and b2 are same as a1 and a2, respectively, but for 2013–09–05 11:20. The 95% significance levels are provided.

using the equation w_{pres}=–$\partial p/\partial t$ (Fig. 3a), where the pressure signals, p, were processed by low-pass filtering for one second. To compare S_{ww}^{ADV} and S_{ww}^{pres}, S_{ww}^{pres} was shifted to the level where the maximum S_{ww}^{pres} within the surface gravity wave-influenced wavenumber band was same as that of S_{ww}^{ADV}. The wave band cutoff wavenumber, k_c, is defined as the wavenumber where S_{ww}^{pres} rises to 30% of S_{ww}^{ADV} (Figs 5a1, b1). The wave band where S_{ww}^{pres} is consistent with S_{ww}^{ADV} is affected by surface gravity waves. At wavenumbers higher than the overlap wave band, S_{ww}^{pres} increases because of sensor noise. The upper inset in Fig. 5 shows that S_{ww}^{ADV} was comparable to the –5/3 slope except for the wavenumber band that was influenced by the gravity surface waves. By multiplying the cospectrum by the wavenumber, k, we find the observed variance-preserving cospectra to be in good agreement with the model cospectra (Figs 5a2, b2), whereas for wavenumbers higher than k_c, the observed cospectra are disordered and depart from the model cospectra. The cutoff wavenumber, k_c, gives the minimum resolved length scale ($\lambda_c = 2\pi/k_c$) of the below-wave band turbulence. In our measurement, the minimum length scale is generally larger than 0.1 m (Fig. 6), which is much smaller than the result of Gerbi et al. (2008). The reason for this is that the water speed was much slower in our case.

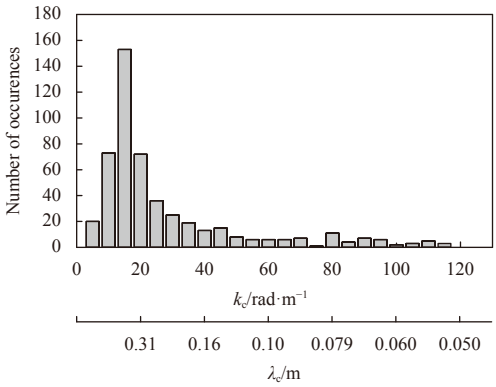

Fig. 6. Histogram of the wave band cutoff wavenumber, k_c, and the corresponding cutoff length scale, λ_c.

Cospectral estimation of turbulent fluxes explained by turbulent motions, $\overline{u'w'}^{model}$ and $\overline{T'w'}^{model}$, were computed by fitting the model cospectrum, shown in Eq. (4), to the observed below-wave band cospectrum. One uncertainty of the cospectral estimation was that the cutoff wavenumber, k_c, falls in the turbulent motion band. In our case, the model fit was limited because k_c was at least twice the model predicted value of k_0, i.e., $k_c > 2k_0$, a criteria that was not met by ~6% of the observed spectra.

By applying the cospectra-fit method, we obtain data that is required to satisfy the Taylor's frozen turbulence hypothesis, whereby the observed results are spatially representative. The frozen turbulence hypothesis must be satisfied in order to convert the measured temporal domain to a spatial domain, such that the spatial patterns of turbulent motion are carried past a fixed point by a convection speed without any essential changes. Gerbi et al. (2008) used the condition of $\frac{\sigma}{U} < 2$ to make this restriction, where σ is the root-mean-square wave velocity and U is the steady drift speed. In this study, 46% of the data did not meet the requirement of $\frac{\sigma}{U} < 2$. However, according to He and Zhang (2006), who studied space-time correlations in turbulent shear flows by using an elliptic model, despite the extreme condition of vanishing mean water flows, the measurements are still spatially representative. The elliptic model expands the space-time correlation function in the Taylor series about the origin up to the second order. Whereas the Taylor's frozen flow hypothesis was achieved by expanding the space-time correlation function with one-order linear approximation. The elliptic model reveals that the space-time correlations are mainly determined by the mean convection velocity and the sweeping velocity. There are two extreme cases of the vanishing sweeping velocity and vanishing mean convection velocity. The study of He and Zhang (2006) indicates that the measurements remain spatially representative under both of these extreme cases in turbulent shear flows. For the first case, the Taylor hypothesis holds that the sweeping velocity is relatively small in comparison to the mean convection velocity. Whereas for the second case, the Taylor hypothesis collapses and is not suitable for illustrating the problem of spatial representation. Thus, in this study, all the data were preserved based on the study of He and Zhang (2006).

3 Results and discussion

3.1 *Quality of cospectra-fit estimates*

Two tests were conducted to evaluate the cospectra-fit results relative to the observations. Firstly, the observed below-wave band variance-preserving cospectrum and the form predicted by Eq. (4) were compared. The cospectral energies are normalized by the model-estimated covariance, $\overline{T'w'}^{model}$ or $\overline{u'w'}^{model}$, and grouped into bins by wavenumber. The wavenumbers are then normalized using the model-estimated roll-off wavenumber estimates k_{0Tw} and k_{0uw}. With the normalizations, estimates of the mean observed below-wave band cospectra fall close to the theoretical model cospectra (Fig. 7).

Secondly, the covariance estimated by the model-fit, $\overline{\beta'w'}^{model}$, and the covariance estimates computed by integrating the measured cospectra below the wave band cutoff, $\overline{\beta'w'}^{int}$, were compared as shown in Eq. (6):

$$\overline{\beta'w'}^{int} = \int_0^{k_c} Co_{\beta w}(k)\,\mathrm{d}k. \tag{6}$$

For the turbulent heat flux, the linear regression slope between the model-fit results and the integrated results was 1.12 and the R^2 was 0.96 (Fig. 8a). For the Reynolds stress, the linear regression slope was 1.13 and the R^2 was 0.93 (Fig. 8b). Both the model-fit estimates of the turbulent heat flux and the Reynolds stress were slightly larger than the integrated estimates. The reason for this was a lack of estimates for the contribution of turbulence in the above-wave band of the cutoff frequency. The results mean that in our measurements, at least 87% of the turbulent covariance was explained by turbulence below the wave band cutoff. The remaining 13% was explained by motions with wavenumbers above the cutoff wave band.

3.2 *The turbulent heat flux and Reynolds stress*

The turbulent flux was calculated in 5 min intervals. This interval was selected because it is sufficient for capturing most of the flux, and because data in a longer time interval would suffer much more easily from non-stationarity conditions. However, stationarity is required for the application of turbulent flux calculation (Tennekes and Lumley, 1972; Katul et al., 2004).

Figure 9 shows the model fitted turbulent heat flux, Q_s, and

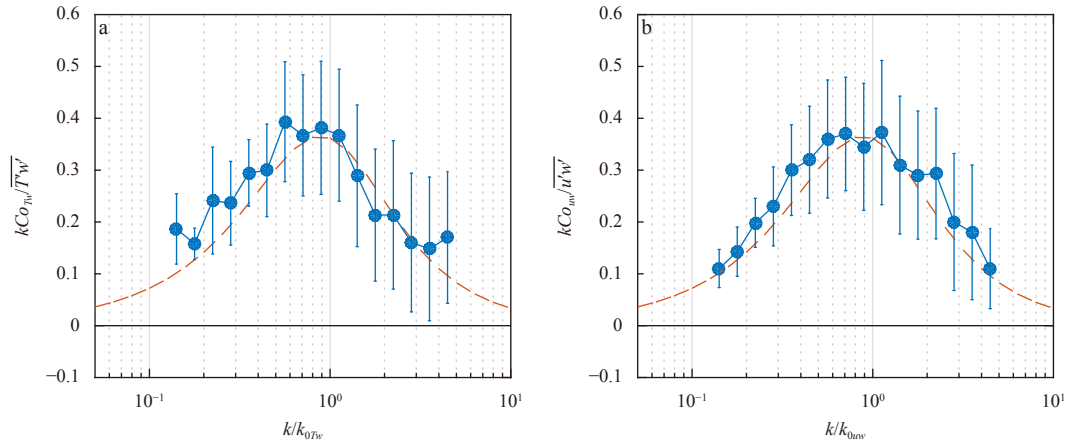

Fig. 7. Bin averages and the standard errors of normalized variance-preserving cospectra. $kCo_{Tw}/\overline{T'w'}$ (a), and $kCo_{uw}/\overline{u'w'}$ (b), in the function of normalized wavenumber k/k_0. Dots indicate the results of observations, and the dashed lines show the model predictions using Eq. (4).

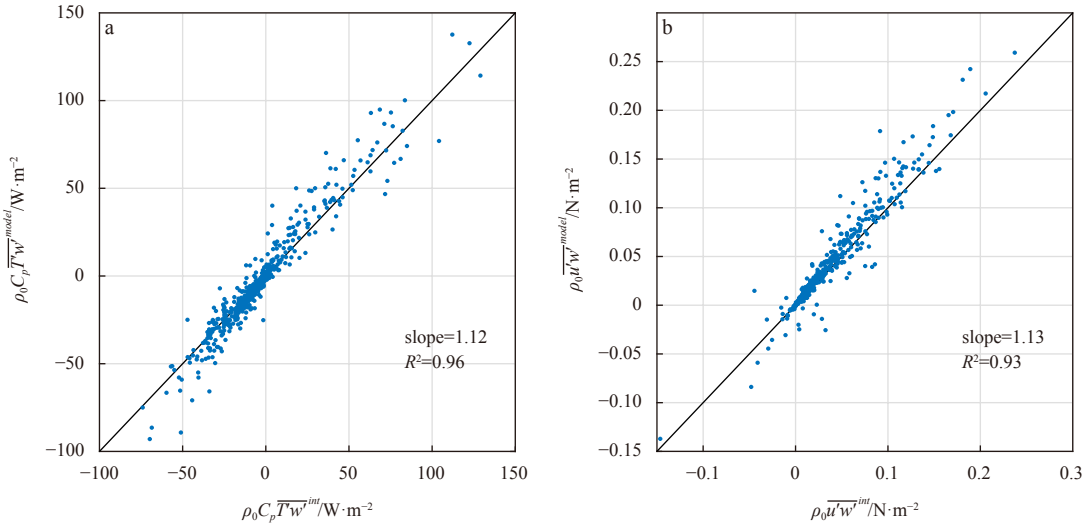

Fig. 8. Comparison of modelled and observed estimates of the turbulent heat flux (a), and the Reynolds stress (b). The linear regression slopes and determination coefficients (R^2) are shown.

the Reynolds stress, τ, in our observation. The turbulent heat flux varied from –70 W/m^2 to 120 W/m^2 with a daily successive variation. There was one positive peak during low tide periods, which lasted from 15:00 to 21:00 on each day when the water level reached the lowest value. In the low tide periods, the mean turbulent heat fluxes were 14.5 and 19.1 W/m^2 for the two days, respectively. Outside of this period there were relatively small turbulent heat fluxes, with mean value of –8.6 W/m^2.

The Reynolds stress values, τ, also showed a daily successive variation. However, this differed from the turbulent heat flux in that the Reynolds stress peaks appeared in the ebb tide period between 12:00 to 18:00 after the water level reached the highest value. The mean peak values of τ were 0.057 N/m^2 and 0.063 N/m^2 for the two days, respectively, with a mean value of 0.02 N/m^2 for the period outside of the ebb tide, which only experienced one-third of the peak periods. The water velocity had the same periodic variation as the Reynolds stress, with a higher water velocity corresponding to greater Reynolds stress and a lower water velocity corresponding to less stress (Fig. 2), thus indicating the energy contribution from the tidal current to the momentum flux.

Figure 10 shows a quadratic functional relationship between the water velocities and the Reynolds stresses, as denoted by Eq. (7):

$$\tau = 10.5U^2 + 0.3U + 0.003. \quad (7)$$

This means that the Reynolds stress increased non-linearly with the velocity in the quadratic relationship.

The heat flux and Reynolds stress varied significantly in the specific time periods, the former peaked during the low tide period and the later peaked during the ebb tide period, thus meaning that they were transported by different scales of turbulence. The roll-off wavenumber, k_0 (Eq. (4)), estimated as part of the model fit to the below-wave band cospectra, represents the horizontal length scales of the dominant flux-carrying eddies. Figure 11 show the histogram of k_0 for the heat flux and the Reynolds stress. This shows most of the k_0 smaller than 10 rad/m and the roll-off wavelengths, λ_0, larger than 0.63 m. The k_0 of the Reynolds stress tended to be larger than that of the heat flux, whereas the λ_0 of the Reynolds stress tended to smaller than that of the heat flux. Since

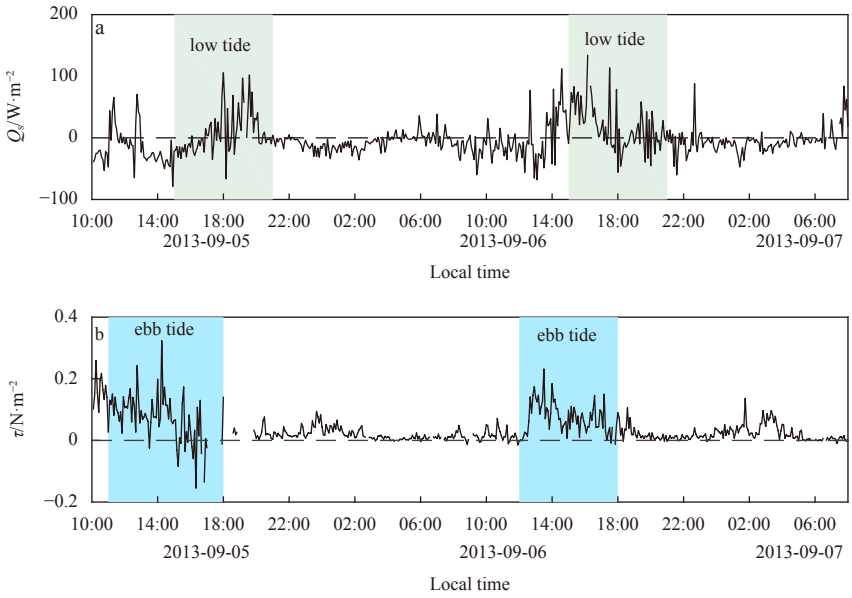

Fig. 9. Estimate of cospectra-fitted turbulent heat flux, Q_s, and Reynolds stress, τ. The corresponding low tide and ebb tide periods are marked.

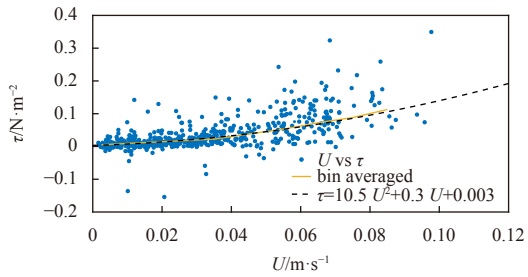

Fig. 10. Plot of Reynolds stress, τ, versus water velocity, U. The yellow line is the bin averaged data of each 0.01 m/s. The dashed line is the quadratic fitting curve of the Reynolds stress.

the eddy covariance system was secured beneath the sea surface, with the water level varying, we can calculate the variation in λ_0 with depth. The λ_0 increases with depth in a departure from the boundary (Fig. 11b), which was similar to previous estimates by Kirincich et al. (2010). Here, the λ_0 of the turbulent heat flux is generally larger than that of the Reynolds stress. For the Reynolds stress, λ_0 was ~1 m at a pressure >1.2 dbar. For the turbulent heat flux, λ_0 was approximately twice that of the Reynolds stress.

3.3 *The relationship between tides and turbulent flux*

During the observation period, the pressure signal recorded by the ADV showed the characteristics of the regular and periodic changes (Fig. 2b). The water level rises and falls twice a day, at higher tide and at low tide, thus indicating the feature of a diurnal tide and semi-diurnal tide. Tides are the basic dynamic characteristics of the ocean. It has been verified that tides can enhance turbulence dissipation and material exchange (Lozovatsky et al., 2008). Whereas the relationship between tides and turbulence flux, including heat flux and Reynolds stress, remains unclear.

To examine these relationships, we analyzed the data with the wavelet analysis method; a major time-frequency decomposition tool for data analysis. The wavelet transform can examine the signal simultaneously in both time and frequency, which is distinctly different from the traditional short-time Fourier transform. The continuous wavelet transform of a discrete sequence

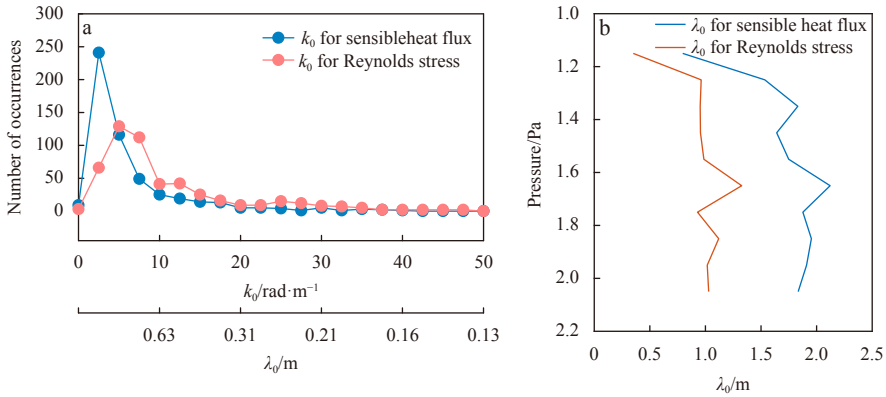

Fig. 11. (a) Histogram of the dominant wavenumber of turbulent fluctuations, k_0, and the corresponding dominant length scale, λ_0, and (b) plots of the averaged λ_0 versus the pressure signal recorded by the ADV.

x_n is defined as the convolution of x_n with the wavelet function $\psi_0(\eta)$ (Torrence and Compo, 1998), as expressed by Eq. (8):

$$W_n^X(S) = \sqrt{\frac{\delta t}{S}} \sum_{n'=0}^{N-1} x_{n'} \psi_0 \left[\frac{(n'-n)\,\delta t}{S} \right], \tag{8}$$

where n is the local time index, δt is the time interval of the signal x_n, and S the wavelet scale. By varying the wavelet scale and translating along the localized time index, one can construct a picture of the amplitude of any features versus the scale, and also of how this amplitude varies with time. The Morl wavelet, $\psi_0(\eta) = \mathrm{e}^{-\frac{\eta^2}{2}} \cos(5\eta)$, was applied for the wavelet analysis in the study.

The zonal velocity, U, was selected as the representative for studying the wavelet analysis (Fig. 12a). Wavelet transforms of the velocity (W^U) are displayed in Fig. 12a corresponding to periods of 1–16 hours. When dealing with finite-length time series, errors (edge effects) will occur at the beginning and end of the wavelet power spectrum. The region affected by edge effects is known as the cone of influence (COI), which is defined as the e^{-2} time for the auto correlation of wavelet power at each scale (Grinsted et al., 2004). The COI is also overlain to highlight the region in which edge effects cannot be ignored. When the COI region was excluded, high wavelet coefficients with a period of ~12 hours (above the 5% significance level), indicated that the high kinetic energy was dominated by a semi-diurnal signal, which is the same as the features recorded by the pressure sensors (Fig. 2b). Wavelet transforms of the measured eddy heat flux (W^Q) and Reynolds stress (W^τ) were also calculated (Figs 12b, c). The highest wavelet coefficients of W^Q correspond to ~11 hours, while the highest wavelet coefficients of W^τ correspond to ~12 hours. The discrepancy between these highest wavelet coefficients is caused by the different scales of eddies that contribute to the turbulent heat flux and Reynolds stress (Fig. 11).

Due to the short time of data acquisition, the edge effects exclude the diurnal tide signals, which are displayed as high wavelet coefficients of semi-diurnal tides. However, there were peaks in a day for both turbulent heat flux and Reynolds stress (Fig. 9), which were during the low tide and ebb tide periods, respectively, thus indicating the diurnal signal. The high correlation between the eddy fluxes and tides suggests that the heat and momentum were transported from the tides to the eddies.

4 Conclusions

The variance method framework for estimating stresses and heat flux transported by eddies from ADV observations could be an important tool for understanding ocean dynamics. However, the direct eddy covariance method is inadequate in estimating the eddy fluxes in the presence of surface gravity waves. Following Gerbi et al. (2008), the cospectra-fit method provided an acceptable way to calculate the Reynolds stresses and turbulent heat fluxes from ADV observations with the effects of surface gravity waves. This method works by fitting an established semi-empirical model of boundary layer turbulence to the measured turbulent cospectra at frequencies below those of surface gravity waves to estimate the stress and heat flux. In this study, as much

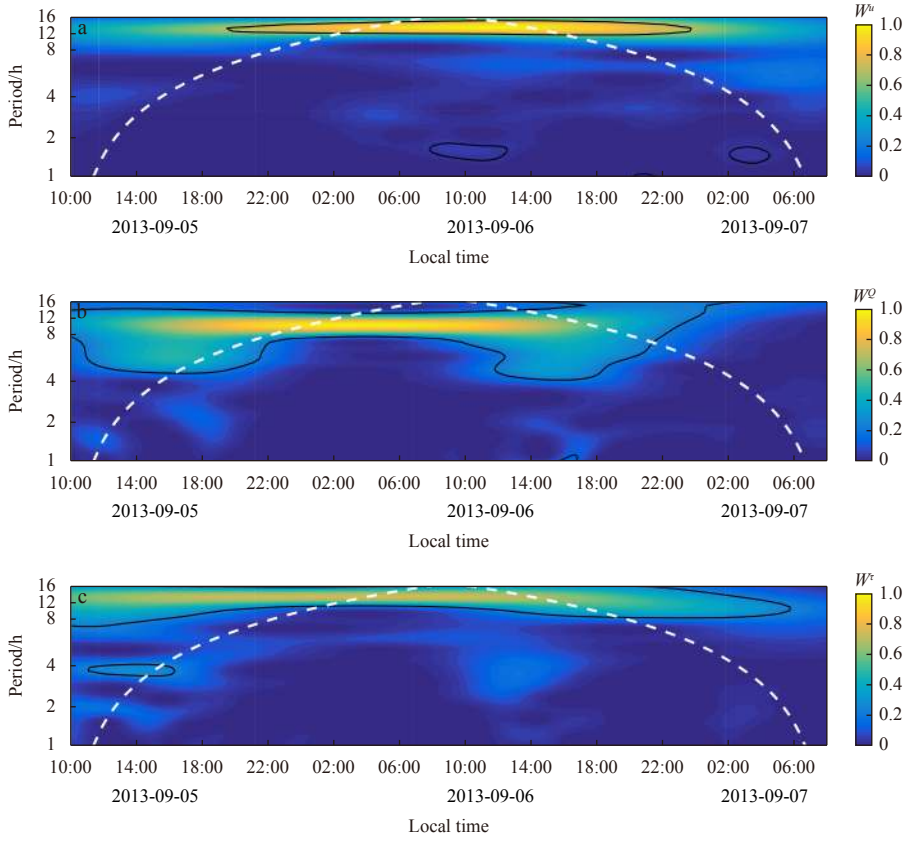

Fig. 12. Modulus of the wavelet transform of zonal velocity u (a), turbulent heat flux Q_s (b) , and Reynolds stress τ (c). The white dashed lines indicate the cone of influence that delimits the region that is not influenced by edge effects. The 5% significance level against red noise in shown as a black contour.

as 87% of the total turbulent stresses and 88% of the total turbulent heat flux existed at frequencies below those of surface gravity waves.

The cospectra-fit method was applied to estimate the Reynolds stresses and turbulent heat flux for a two-day observation made at a depth of ~1.5 m beneath the sea surface at the coast of Sanya, China. The observation system consisted of an ADV and a fast temperature sensor. The results show that the turbulent heat varied from –70 W/m^2 to 120 W/m^2 and that the Reynolds stress varied from –0.15 N/m^2 to 0.3 N/m^2. Both the turbulent heat flux and Reynolds stress had a daily successive variation, peaking during the low tide periods that follow the highest water level and during the ebb tide periods after the spring tide, respectively. The discrepancy between the peak periods for the turbulent heat flux and Reynolds stress indicates the differing scales of eddies that contributed to them. The roll-off wavenumbers, k_0, and roll-off wavelengths, λ_0 (where $\lambda_0 = 2\pi/k_0$), that were derived from the cospectra-fit method, estimate the horizontal length scales of the dominant flux-carrying turbulent eddies. The λ_0 of the turbulent heat flux was approximately double that of the Reynolds stress.

Wavelet analysis was applied to study the relationship between the turbulent heat flux and Reynolds stress and large-scale tides. Both the turbulent heat flux and Reynolds stress showed a close relationship to the semi-diurnal and diurnal tides, and therefore indicate the energy that is transported from tides to turbulence.

Acknowledgements

We thank the Guangzhou Ouna Electronic Technology Co., Ltd for providing the technical support for developing the eddy covariance system.

References

Berg P, Glud R N, Hume A, et al. 2009. Eddy correlation measurements of oxygen uptake in deep ocean sediments. Limnology and Oceanography, 7(8): 576–584

Berg P, Røy H, Janssen F, et al. 2003. Oxygen uptake by aquatic sediments measured with a novel non-invasive eddy-correlation technique. Marine Ecology Progress Series, 261: 75–83, doi: 10.3354/meps261075

Berg P, Røy H, Wiberg P L. 2007. Eddy correlation flux measurements: the sediment surface area that contributes to the flux. Limnology and Oceanography, 52(4): 1672–1684, doi: 10.4319/lo.2007.52.4.1672

Bowden K F, Fairbairn L A. 1956. Measurements of turbulent fluctuations and Reynolds stresses in a tidal current. Proceedings of the Royal Society A: Mathematical, Physical and Engineering Sciences, 237(1210): 422–438

Crusius J, Berg P, Koopmans D J, et al. 2008. Eddy correlation measurements of submarine groundwater discharge. Marine Chemistry, 109(1–2): 77–85, doi: 10.1016/j.marchem.2007.12.004

Gerbi G P, Trowbridge J H, Edson J B, et al. 2008. Measurements of momentum and heat transfer across the air-sea interface. Journal of Physical Oceanography, 38(5): 1054–1072, doi: 10.1175/2007JPO3739.1

Grinsted A, Moore J C, Jevrejeva S. 2004. Application of the cross wavelet transform and wavelet coherence to geophysical time series. Nonlinear Processes in Geophysics, 11(5–6): 561–566

He Guowei, Zhang Jinbai. 2006. Elliptic model for space-time correlations in turbulent shear flows. Physical Review E, 73(5): 055303, doi: 10.1103/PhysRevE.73.055303

Heathershaw A D. 1979. The turbulent structure of the bottom boundary layer in a tidal current. Geophysical Journal International, 58(2): 395–430, doi: 10.1111/j.1365-246X.1979.tb01032.x

Kaimal J Y, Izumi J C, Cote O R. 1972. Spectral characteristics of surface-layer turbulence. Quarterly Journal of the Royal Meteorological Society, 98: 563–589, doi: 10.1002/qj.49709841707

Katul G, Cava D, Poggi D, et al. 2004. Stationarity, homogeneity, and ergodicity in canopy turbulence. In: Lee X H, Massman W, Law B, eds. Handbook of Micrometeorology: A Guide for Surface Flux Measurement and Analysis. Dordrecht: Springer, 84–102

Kirincich A R, Lentz S J, Gerbi G P. 2010. Calculating Reynolds stresses from ADCP measurements in the presence of surface gravity waves using the cospectra-fit method. Journal of Atmospheric and Oceanic Technology, 27(5): 889–907, doi: 10.1175/2009JTECHO682.1

Kuwae T, Kamio K, Inoue T, et al. 2006. Oxygen exchange flux between sediment and water in an intertidal sandflat, measured *in situ* by the eddy-correlation method. Marine Ecology Progress Series, 307: 59–68, doi: 10.3354/meps307059

Lozovatsky I, Liu Zhiyu, Wei Hao, et al. 2008. Tides and mixing in the northwestern East China Sea, Part II: near-bottom turbulence. Continental Shelf Research, 28(2): 338–350, doi: 10.1016/j.csr.2007.08.007

Mei C C. 1989. The Applied Dynamics of Ocean Surface Waves. Singapore: World Scientific, 760

Priestley C H B, Swinbank W C. 1947. Vertical transport of heat by turbulence in the atmosphere. Proceedings of the Royal Society A: Mathematical, Physical and Engineering Sciences, 189(1019): 543–561

Reimers C E, Özkan-Haller H T, Berg P, et al. 2012. Benthic oxygen consumption rates during hypoxic conditions on the Oregon continental shelf: evaluation of the eddy correlation method. Journal of Geophysical Research, 117(C2): C02021, doi: 10.1029/2011JC007564

Shang X D, Qiu X L, Tong P, et al. 2003. Measured local heat transport in turbulent Rayleigh-Bénard convection. Physical Review Letters, 90(7): 074501, doi: 10.1103/PhysRevLett.90.074501

Shang X D, Qiu X L, Tong P, et al. 2004. Measurements of the local convective heat flux in turbulent Rayleigh-Bénard convection. Physical Review E, 70(2): 026308, doi: 10.1103/PhysRevE.70.026308

Shaw W J, Trowbridge J H. 2001. The direct estimation of near-bottom turbulent fluxes in the presence of energetic wave motions. Journal of Atmospheric and Oceanic Technology, 18(9): 1540–1557, doi: 10.1175/1520-0426(2001)018<1540:TDEONB>2.0.CO;2

Soulsby R. 1980. Selecting record length and digitization rate for near-bed turbulence measurements. Journal of Physical Oceanography, 10: 208–219, doi: 10.1175/1520-0485(1980)010<0208:SRLADR>2.0.CO;2

Tennekes H, Lumley J L. 1972. A First Course in Turbulence. Cambridge: MIT Press, 27–34

Torrence C, Compo G P. 1998. A practical guide to wavelet analysis. Bulletin of the American Meteorological Society, 79(1): 61–78, doi: 10.1175/1520-0477(1998)079<0061:APGTWA>2.0.CO;2

Trowbridge J H. 1998. On a technique for measurement of turbulent shear stress in the presence of surface waves. Journal of Atmospheric and Oceanic Technology, 15(1): 290–298, doi: 10.1175/1520-0426(1998)015<0290:OATFMO>2.0.CO;2

Trowbridge J, Scully M, Sherwood C R. 2018. The cospectrum of stress-carrying turbulence in the presence of surface gravity waves. Journal of Physical Oceanography, 48(1): 29–44, doi: 10.1175/JPO-D-17-0016.1

Warner J C, Sherwood C R, Arango H G, et al. 2005. Performance of four turbulence closure models implemented using a generic length scale method. Ocean Modelling, 8(1–2): 81–113, doi: 10.1016/j.ocemod.2003.12.003

Wyngaard J, Coté O. 1972. Cospectral similarity in the atmospheric surface layer. Quarterly Journal of the Royal Meteorological Society, 98: 590–603, doi: 10.1002/qj.49709841708

Yamamoto S, Kayanne H, Tokoro T, et al. 2015. Total alkalinity flux in coral reefs estimated from eddy covariance and sediment porewater profiles. Limnology and Oceanography, 60(1): 229–241, doi: 10.1002/lno.10018